Journal of
Marine Science and Engineering

MDPI

Article

Typhoon-Triggered Phytoplankton Bloom and Associated Upper-Ocean Conditions in the Northwestern Pacific: Evidence from Satellite Remote Sensing, Argo Profile, and an Ocean Circulation Model

Joon-Ho Lee [1], Jae-Hong Moon [2,*] and Taekyun Kim [2]

[1] Basic Science Institute, Jeju National University, 102 Jejudaehak-ro, Jejusi 63243, Korea; ocean0510@gmail.com
[2] Department of Earth and Marine Science, Jeju National University, 102 Jejudaehak-ro, Jejusi 63243, Korea; tkkim79@gmail.com
* Correspondence: jhmoon@jejunu.ac.kr; Tel.: +82-64-754-3432

Received: 18 September 2020; Accepted: 8 October 2020; Published: 10 October 2020

Abstract: A long-lasting phytoplankton bloom, characterized by high chlorophyll-a (Chl-a) concentrations in an eddy-like feature, was detected in MODIS satellite imagery of the northwestern Pacific following the passage of Typhoon Krosa in August 2019. Satellite datasets, Argo measurements, and regional ocean models were analyzed to determine the occurrence and abundance of high-Chl-a concentrations and the upper-ocean conditions associated with them before and after the passage of the typhoon. Remote sensing data revealed that the typhoon triggered sharp increases in surface Chl-a concentrations more than five times the pre-typhoon average, which lasted for two weeks. The elevated post-typhoon concentrations coincided with a pre-existing oceanic cyclone that was detected as an altimetry-based sea surface height anomaly. The typhoon looped around the oceanic cyclone and lingered for two days at slow speeds (less than 2 m/s), producing an unusual sea-surface cooling of up to approximately 9 °C in the cyclonic eddy region. Our model successfully captured the typhoon-induced cold-core cyclonic circulation, which corresponded to the region of high Chl-a concentration. Model–data comparisons revealed that the looping motion of the slow-moving typhoon enhanced the pre-existing cyclonic circulation, resulting in strong vertical mixing and upwelling, consequently initiating a phytoplankton bloom due to increased nutrient supply to the euphotic zone.

Keywords: phytoplankton bloom; typhoon; cyclonic eddy; vertical mixing and upwelling; MODIS satellite

1. Introduction

Chlorophyll-a (Chl-a) concentration is an index of phytoplankton bloom on the ocean surface that plays a crucial role in the air–sea carbon cycle, a major climate-regulating factor [1,2]. Chl-a concentration is also an important environmental monitoring tool in ecological and fishery management [3,4], making it an important parameter in a number of fields of research, including the study of oceanic ecosystems and biogeochemical cycles.

The strong winds associated with typhoons cause vertical mixing and upwelling in the tropical and subtropical regions, which in turn cool the sea surface and deepen the ocean mixed layer along the storm track [5,6]. Typhoon-induced upwelling and/or vertical mixing (entrainment) can raise nutrient-rich waters from the subsurface below the mixed layer up to the euphotic layer, fueling photosynthesis and inducing the large-scale growth of phytoplankton that can be observed using

remote-sensed Chl-a products [7–9]. The MODIS satellite data are widely used to produce higher resolution images of phytoplankton concentration [7–10].

A large number of typhoons pass over the subtropical northwestern Pacific region, which spawn approximately 30% of the world's tropical cyclones [10]. In the subtropical regions, Chl-a concentration is low in the near-surface layer and gradually increases with depth, reaching a maximum near the bottom of the euphotic layer (100–120 m). The upper-ocean layer is well stratified and the mixed layer depth is shallower than the euphotic layer throughout the year. For these reasons, strong phytoplankton blooms are rarely detected in the subtropical regions despite the relatively more frequent cooling of sea surface temperature (SST) following typhoon passage [11]. Strong blooms of phytoplankton are occasionally detected when slow-moving typhoons linger over a region [12].

An eddy-like phytoplankton bloom with high concentrations of Chl-a was observed in remote sensing images of the northwestern Pacific following the passage of Typhoon Krosa in August 2019 (Figure 1). The strong bloom began in the looping area of the typhoon on 12 August 2019 and lasted for approximately two weeks following the typhoon's passage. Similar rare blooms in the subtropical region were observed during the passages of Typhoon Keith in November 1997 and Typhoon Ketsana in October 2003. Shibano et al. [11] reported that a patch-like phytoplankton bloom occurred around one of the recurvature points of Typhoon Keith, reflecting the role of typhoon-induced upwelling and biogeochemical processes in determining phytoplankton growth following typhoon passage. Using satellite observations and ocean model simulation, Yin et al. [13] determined that the cyclonic circulation associated with Typhoon Ketsana pumped cold, nutrient-rich subsurface waters up to the sea surface, producing SST cooling and high concentrations of Chl-a at the surface. Due to observational difficulties, in-situ measurements of the water column were not possible during Typhoons Keith and Ketsana.

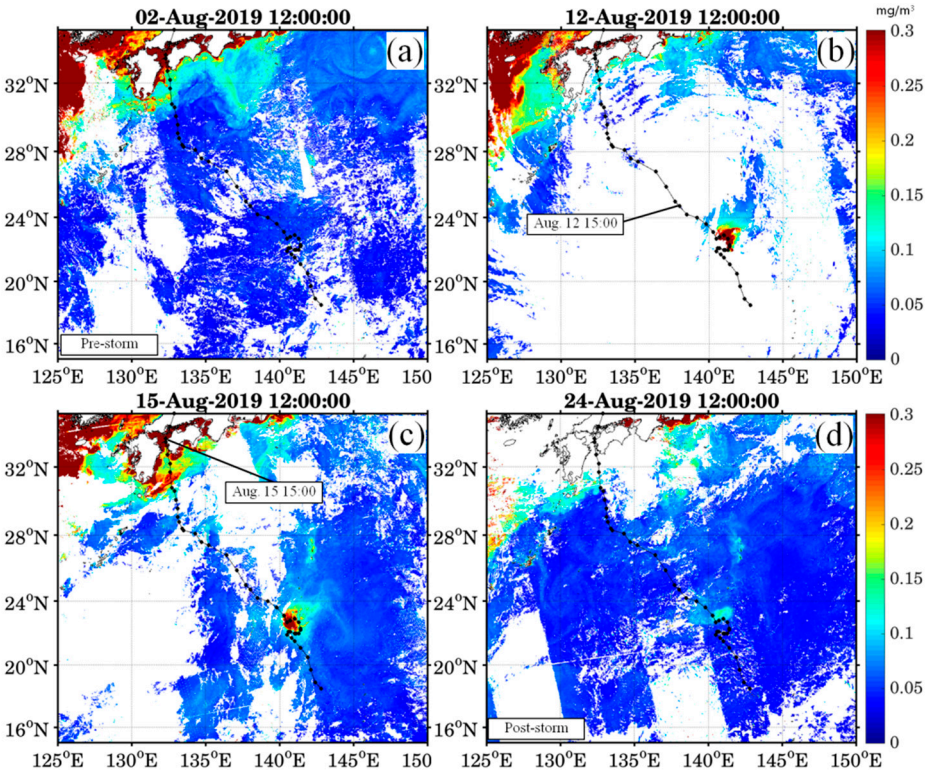

Figure 1. Distributions of surface Chl-a concentrations before and after passage of Typhoon Krosa in August 2019: (**a**) 2 August, (**b**) 12 August, (**c**) 15 August, and (**d**) 24 August 2019.

In this study, we identified the surface phytoplankton bloom initiated by Typhoon Krosa in 2019 and determined the associated upper-ocean conditions before and after passage of the typhoon based on an analysis of satellite datasets, Argo data, and the output of a regional ocean circulation model.

Argo measurement, which is not limited by severe weather conditions, can provide observational evidence for detailed ocean state structures during typhoon passage. In particular, we demonstrate that the two independent observational sets (i.e., remote sensing and Argo data) and the ocean model simulation results provide a consistent explanation of the upper-ocean responses to Typhoon Krosa and the associated eddy-like phytoplankton bloom at the sea surface.

2. Data and Model

2.1. Data

2.1.1. Remote Sensing and Argo Profiles Data

The Chl-a data derived from the MODIS sensors aboard the Aqua and Terra satellites were used to investigate the spatial and temporal changes in surface Chl-a concentration before and after the passage of Typhoon Krosa. The Chl-a concentration is calculated using the OC3 chlorophyll algorithm in the MODIS product. To carry out the analysis, we used the three-day average sea surface Chl-a concentration data with a spatial resolution of 4 km, which were merged using the MODIS Aqua and MODIS Terra Level 3 products (http://oceancolor.gsfc.nasa.gov). The sea surface response to the typhoon was identified by analyzing the optimally interpolated (OI) cloud-free satellite SST products, which were provided by remote sensing systems (REMSS, http://www.remss.com). The REMSS SST data were produced using satellite measurements from the Tropical Rainfall Measuring Mission Microwave Imager (TMI) and the Advanced Microwave Scanning Radiometers of the Earth Observing System satellites (AMSR-E and AMSR2). The data were interpolated to fill in gaps arising from orbit transition and other environmental factors to achieve a 0.1° resolution (~10 km). The AMSR SST measurements were used to supplement the OI REMSS product in validating and calibrating the OI SST product. To detect the oceanic mesoscale circulation during typhoon passage, we used the multi-mission altimeter daily sea surface height anomaly (SSHA) data obtained from the Copernicus Marine and Environment Monitoring Service (https://resources.marine.copernicus.eu). The data were processed on a grid with a spatial resolution of 0.25° × 0.25°.

Argo is an array of active profiling floats that measure the temperature and salinity profiles in the upper 2000 m of the ocean. The target spatial coverage of Argo is one float per 3° latitude and longitude grid cell over the global ocean. The Argo floats have a 10-day overall cycle and temperature and salinity accuracies of 0.002 °C and 0.005 psu (practical salinity unit), respectively. Argo float data have been widely used in many studies describing ocean warming [14] and the response to tropical cyclones [15]. To explore the ocean response to the typhoon, in this study we used the temperature and salinity profile of Argo float 2903334, the closest float to the looping area of Typhoon Krosa. On 23 June 2019, this float was located at 144.85E, 24.19N; further information for the float can be found on the Jamstec website (http://www.jamstec.go.jp/ARGORC/float_inf/meta_inf.php?wmo=2903334). The track of Argo during passage of the typhoon is shown in Figure 2b.

2.1.2. Typhoon Data

The best track data for Typhoon Krosa were obtained from the typhoon center of the Korea Meteorology Administration (https://www.weather.go.kr/weather/typoon/report.jsp). These data were used to identify the translation and intensity of Typhoon Krosa and included the maximum sustained wind speed at sea surface and the location of the typhoon center at 6-hr intervals. The translation speed of the typhoon could be calculated by dividing the distance between each typhoon center location by this time interval. Typhoon Krosa developed from a tropical depression into a tropical storm near the Mariana Islands on 5–6 August 2019 (Figure 2a). The tropical storm soon became a typhoon and rapidly intensified to Category 3 (on the Saffir-Simpson tropical cyclone scale) near the region of 22.0° N and 140.5° E on 8–9 August. During this period, the typhoon made an anticlockwise looping track and lingered for two days with a maximum wind speed of ~43 m/s (Figure 2b,c). As it looped

over the course of these two days, the typhoon produced a minimum translation speed of less than ~2 m/s on 8 August. Krosa then continued moving toward Japan with little change in intensity and on 16 August transitioned into an extratropical low after passing over Japan.

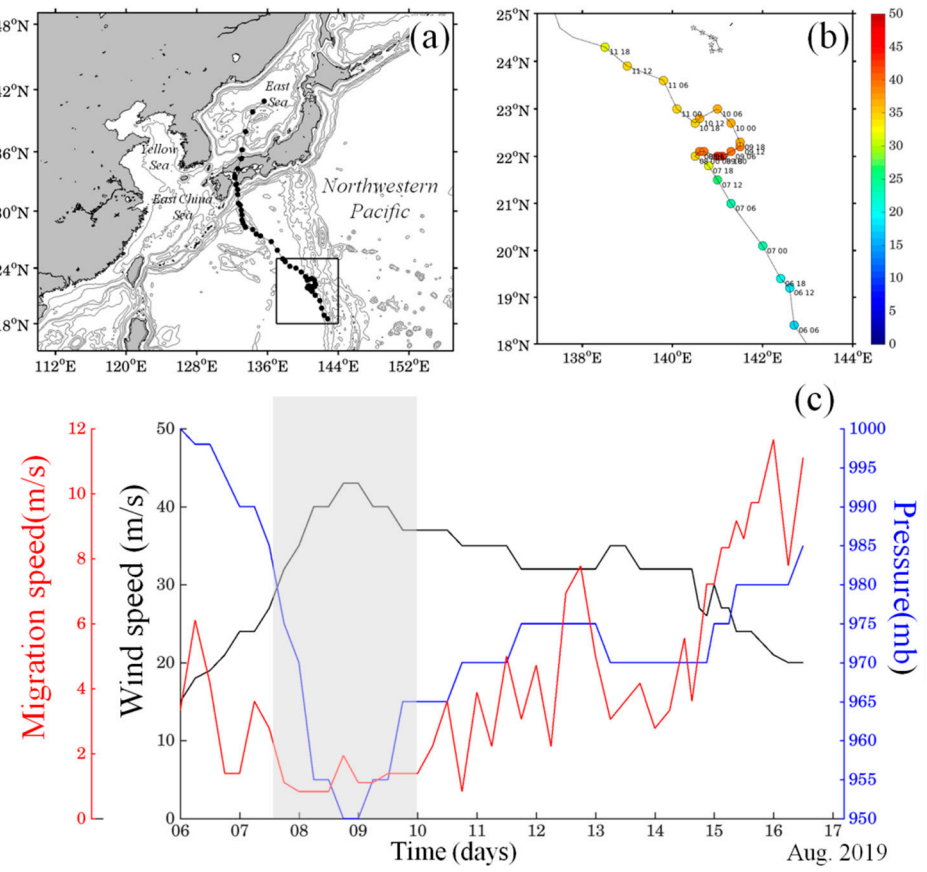

Figure 2. (**a**) Model domain, (**b**) enlarged typhoon track showing wind speed (m/s, colored circles) and Argo track (asterisk), and (**c**) time series of typhoon information along the track. Shaded area indicates the period of typhoon passage.

2.2. Model

The ocean model used in this study was based on the Regional Ocean Modeling System (ROMS), a typical three-dimensional, free-surface, stretched terrain-following coordinate model that solves Reynolds-averaged Navier–Stokes equations [16,17]. The model domain covered the northwestern Pacific from 15° N to 49° N and 110° E to 157° E (Figure 2a). The horizontal resolution of the model was approximately 8 km, and a depth of 36 vertical layers was used in our application. The bathymetry was extracted from a combination of two topographic data sets: the General Bathymetric Chart of the Ocean and Korea Bathymetry 30 [18]. A quadratic bottom friction law with a drag coefficient of 0.0025 was applied in the modeling [19].

The model was one-way nested within the global Hybrid Coordinate Ocean Model (HYCOM) with nominal horizontal and vertical resolutions of 12 km and 40 layers, respectively. The initial states were obtained from the daily mean HYCOM velocity, SSH, temperature, and salinity data on 31 July 2019. Using these initial condition variables, the lateral boundary condition was obtained from the daily mean values of the HYCOM solution from July to August 2019. In ROMS, the surface boundary conditions were calculated using bulk formulas [20] with surface forcing obtained from the National Center for Environmental Prediction (NCEP) FiNal anaLysis (FNL) data, which have a horizontal resolution of 0.125° × 0.125° and a 1-h time interval. The Generic Length Scale mixing scheme, which applies the k-kl method, was used as a vertical mixing parameterization [21]. A total of

10 tidal components (M2, S2, N2, K2, K1, O1, P1, Q1, Mf, and Mm) provided by the TOPEX/POSEIDON (TPXO) 7-atlas were imposed to produce real-time tidal currents and sea level heights [22].

3. Distribution of Surface Chl-a Concentration and SST

Remote sensing data were used to obtain the spatial and temporal evolution of surface Chl-a concentrations during the passage of Typhoon Krosa. One week before typhoon passage (on 2 August 2019, Figure 1a), the surface Chl-a concentration was generally low over the northwestern Pacific, including in the study area. This low concentration is fairly consistent with values commonly observed in subtropical regions [11]. Following typhoon passage, a high concentration of Chl-a appeared in the study area as an eddy-like feature and is assumed to represent a phytoplankton bloom.

The concentration of Chl-a significantly increased in the looping area of the typhoon, achieving a maximum value of >0.3 mg/m^3 one day after the typhoon passed over the area (Figure 1b). This surface Chl-a feature lasted for approximately two weeks thereafter, although at a reduced concentration (Figure 1d). The changes in surface Chl-a concentration before and after typhoon passage are clearly visible in Figure 3, which shows the temporal evolution of Chl-a concentration spatially averaged over the patch region (140–142° E, 20–21.5° N). The relatively low Chl-a concentration of ~0.05 mg/m^3 observed prior to typhoon passage (2–6 August) increased substantially to an area-averaged value of ~0.28 mg/m^3 just after the typhoon (on 12 August), an increase by a factor of more than five. The enhanced Chl-a concentration decreased gradually, reaching its normal level two weeks after the typhoon.

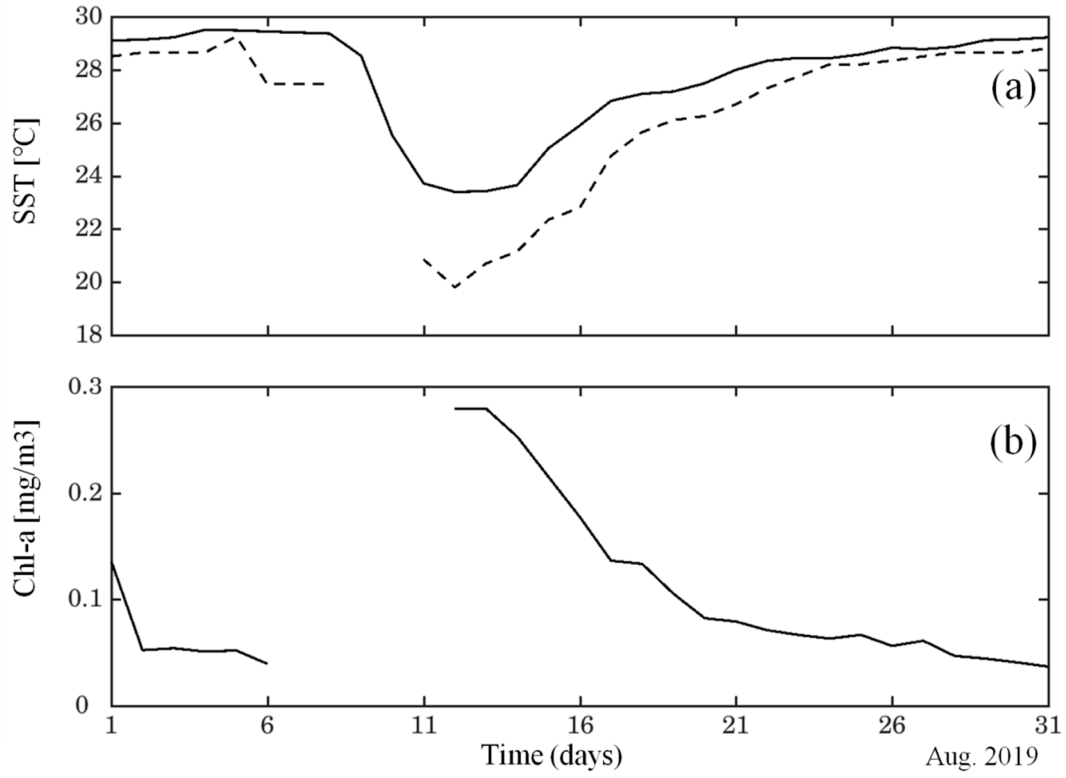

Figure 3. Spatially averaged (140–142° E, 20–21.5° N) time series of (**a**) REMSS (single black line) and AMSR SST (dashed line) and (**b**) Chl-a concentration in August 2019.

Two satellite-based SST products revealed a strong SST cooling during typhoon passage that was accompanied by an increase in sea surface Chl-a concentration. Prior to the typhoon, the water temperature at the surface in the study area was approximately 28–29 °C. As the typhoon approached the study area, the SST rapidly decreased before returning gradually to the pre-typhoon level two

weeks after passage. The REMSS and AMSR products measured maximum post-passage changes in SST of approximately 6 and 9 °C, respectively. This abrupt SST drop provides evidence for entrainment into the warm surface of cold subsurface water from below the thermocline by typhoon-induced strong vertical mixing and upwelling.

4. Upper-Ocean Conditions before and after Typhoon Krosa

4.1. Pre-Existing Cyclonic Circulation

The spatial patterns of remote-sensed SST and altimetry-based SSHA in the study area were analyzed to determine the sea surface conditions before and after typhoon passage (Figure 4). Because the AMSR SST product had a substantial amount of missing data during the passage of Krosa, we used the REMSS SST alone to examine the spatial SST evolution over time. As Typhoon Krosa passed through the Northwest Pacific it induced strong sea surface cooling which appeared in satellite imagery as an eddy. Prior to the typhoon, the SST was high (>28 °C) over most of the study area owing to strong summer heating (Figure 4a). During passage, the SST decreased significantly within the looping area of the typhoon, corresponding to the region in which there were robust Chl-a concentrations (Figure 4b). The patch continued to rapidly expand between August 10–13. Following typhoon passage, the SST gradually increased to pre-typhoon values (Figure 4d–f), with the surface Chl-a concentration following the same trend.

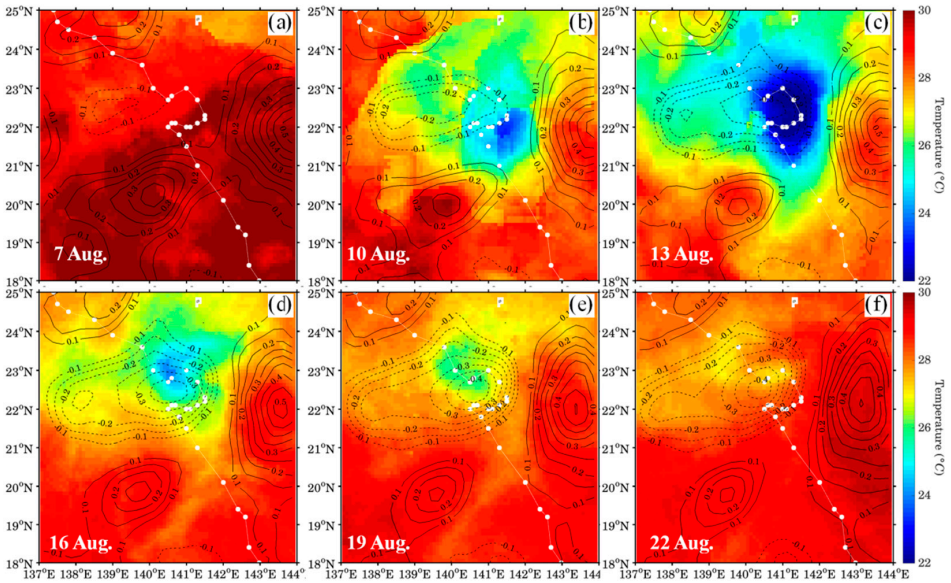

Figure 4. Spatial distributions of observed SST (color) and SSHA (contour) before and after passage of Typhoon Krosa from (**a**) 7 August to (**f**) 22 August 2019 with 3-day interval. The contour interval is 0.05 m. Typhoon track is also displayed shown by a thin line with white circle.

Of particular interest is the presence of a mesoscale cyclonic circulation in the study area before the typhoon approached, as detected by the altimetry-based SSHA (contour lines in Figure 4). This pre-existing cyclonic circulation (i.e., negative SSHA) was located slightly to the west of the looping area of the typhoon on 7 August 2019 (Figure 4a). As the typhoon looped in the region (10–13 August), the cyclonic circulation began to enhance in line with the growth of the cold patch (Figure 4b,c) and continued to do so even two weeks after typhoon passage (Figure 4d–f). Thus, the altimetry-derived SSHA data indicate that the typhoon enhanced the pre-existing cyclonic circulation in the study area during looping.

To further examine the typhoon-enhanced cyclonic circulation, simulated SST, SSHA, and surface current patterns were analyzed (Figure 5). Overall, the simulated typhoon-induced sea surface

cooling was overestimated relative to the SST obtained from the REMSS merged product. Note that, as mentioned previously, the AMSR SST product SST was in closer agreement with the cold SST obtained from the model (not shown here because some data around the study area are missing). Despite the overestimation of SST cooling, the SST and SSHA spatial patterns and temporal evolutions closely match those obtained from satellite-based observations. Our model reproduced the pre-existing cyclonic circulation on the western side of the looping area prior to typhoon approach (7 August, Figure 5a). The cyclonic circulation became more vigorous and grew in size with SST cooling as the typhoon lingered and looped over the study area (7–13 August, Figure 5b,c). A typhoon that moves in this manner can cause cyclonic circulation as a result of the inducement of strong cyclonic winds, which produce surface water divergence at their center accompanied by an upwelling of subsurface cold water. By looping and lingering, Typhoon Krosa further enhanced the pre-existing cyclonic circulation, causing an abrupt reduction in SST as a result of intense vertical mixing and upwelling. The typhoon-enhanced cyclonic circulation persisted up to two weeks after typhoon passage (Figure 5d–f), with the resulting enhanced upwelling bringing nutrient-rich water from the deep layer up to the surface layer and fueling a sea surface phytoplankton bloom in the study area.

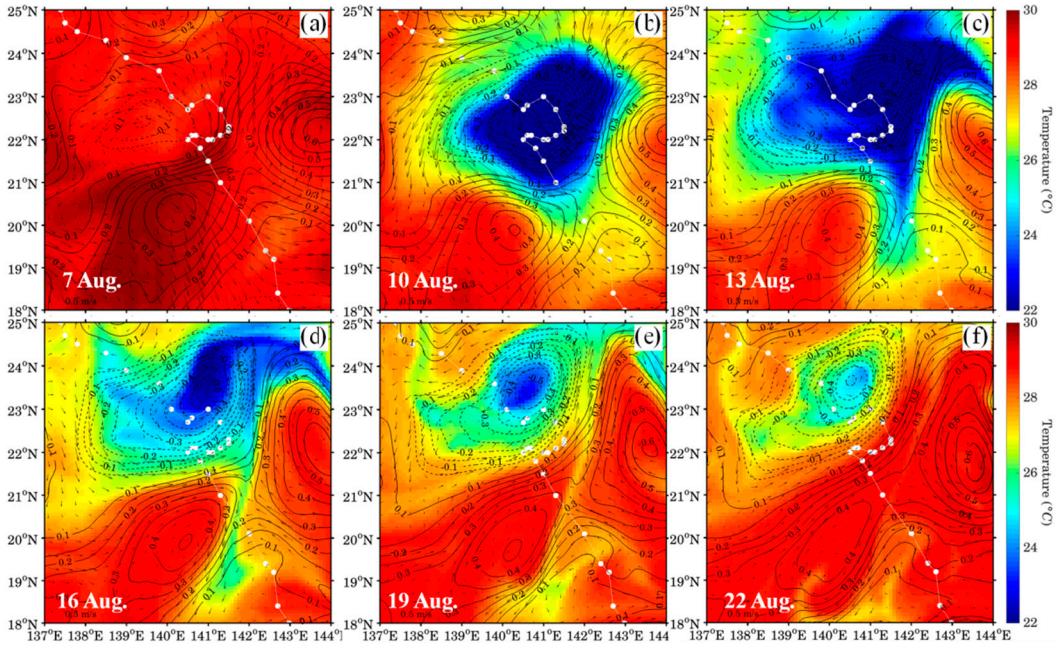

Figure 5. Spatial distributions of model-simulated SST (color), SSHA (contour), and velocities (vector) before and after passage of Typhoon Krosa from (**a**) 7 August to (**f**) 22 August 2019 with 3-day interval. The contour interval is 0.05 m. Typhoon track is also displayed shown by a thin line with white circle.

Our model–data comparisons suggest that a slow-moving typhoon with a looping motion can intensify a pre-existing oceanic cyclone, thereby producing an enhanced upwelling and vertical mixing, a result that is fairly consistent with the results of previous studies [23,24]. This typhoon-enhanced upwelling and vertical mixing can trigger a phytoplankton bloom through an increase in nutrient supply to the surface layer. These results highlight the importance of pre-existing oceanic circulation and the role of typhoon motion in the enhancement of Chl-a concentrations in the subtropical regions.

4.2. Vertical Mixing and Upwelling

Figure 6a shows a time-depth diagram of temperature observed by the Argo float as it drifted around the northern side of the looping area (140–141° E, 24–25° N) of the typhoon. It should be noted that, although the Argo float confirmed the SST cooling shown in the remote-sensed images, it did not measure a surface Chl-a feature. During the tracking period of 29 July–28 August 2019, the float

sampled the upper 2000 m of the water column near the cooling area. The data collected along the Argo float track clearly reveal a distinct change in temperature over the upper water column during the period before and after typhoon passage. From early August and prior to the typhoon's approach, the surface temperature started to gradually decline from 29 °C before sharply decreasing to 26 °C during typhoon passage. The water temperature reached a minimum value from 11–13 August as a result of typhoon-induced vertical mixing in which the mixed layer of the upper ocean deepened to ~60 m, or approximately twice its pre-typhoon depth. Following typhoon passage, the water temperature in the mixed layer became continuously stratified over time as a result of strong surface heating in summer. The presence of well-mixed water in the upper layer during typhoon passage is evident in the Argo-measured density structure shown in Figure 6b. Despite the high degree of mixing in the upper ocean layers, however, the water temperature below the thermocline remained very close to 22 °C during typhoon passage, indicating that the subsurface cold water upwelling was not intense over the Argo track area, in which there was no surface Chl-a surface feature.

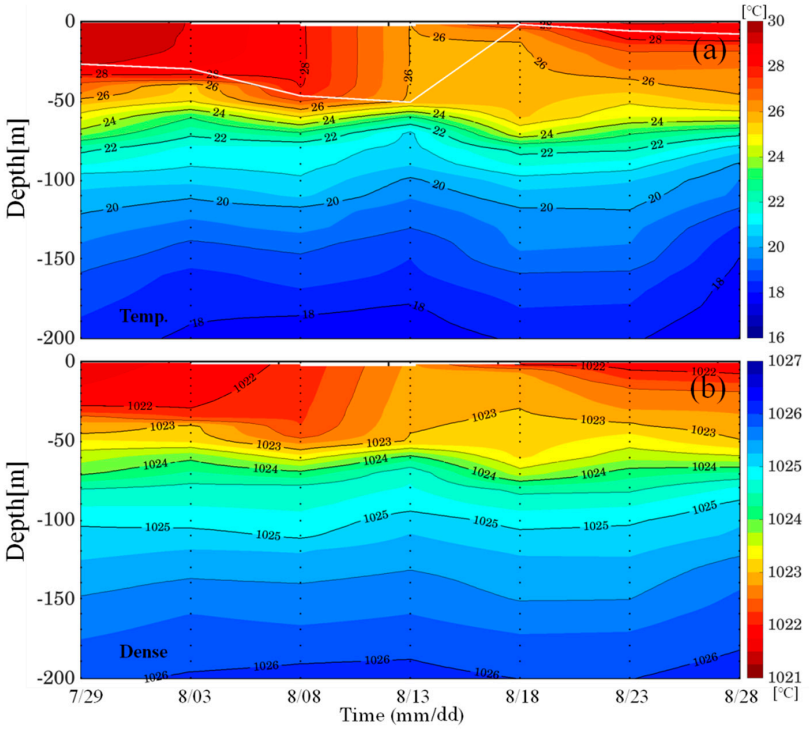

Figure 6. Time–depth diagram of ARGO (2903334) (**a**) temperature and (**b**) density measurements from 29 July to 28 August 2019.

To better understand the role of these physical processes on the surface Chl-a feature, we used model simulation results (Figure 7) to analyze the dynamical responses of the upper ocean to Typhoon Krosa over the sections of the looping area in which surface Chl-a bloom occurred. The modeled temporal changes in the average area temperatures confirmed the presence of strong vertical mixing in the upper layer and intense upwelling over the water column below the thermocline during typhoon passage (Figure 7a). Prior to the typhoon, high temperatures of above 29 °C were distributed over the surface layer; these decreased sharply to 24 °C during typhoon passage (9–12 August), deepening the mixed layer in the upper ocean. These changes in the upper ocean are quite similar to those observed over the Argo track area; unlike in the Argo track area data, however, the water temperature below the thermocline varied largely with time owing to the intense upwelling of subsurface cold water. These differing characteristics of the two layers can be readily obtained from the following temperature diagnostic equation terms:

$$\frac{\partial T}{\partial t} = -\left(\frac{\partial (uT)}{\partial x} + \frac{\partial (vT)}{\partial y} + \frac{\partial (wT)}{\partial z}\right) + k_h \nabla_h^2 T + k_z \frac{\partial^2 T}{\partial z^2} \quad (1)$$

where T is the model temperature, t is time, (u, v, w) are the ocean current components, and k_h and k_z are the horizontal and vertical diffusivity coefficients, respectively. The first two terms on the right-hand side of the equation represents the horizontal advection of T, while the third term represents the vertical advection and the fourth and fifth terms represent the horizontal and vertical diffusions, respectively. As expected, the largest change in temperature rate was found to occur while the typhoon looped and lingered (9–11 August), during which there was a significant degree of cooling over the entire water column (Figure 7b). In this case, the dominant components in Equation (1) were the horizontal and vertical advection terms, whose values were one order of magnitude higher than the other terms (Figure 7c,d). However, these two dominant terms mostly cancelled each other except in the lower layer (Figure 7e), in which there were strong negative values during typhoon passage (9–11 August) corresponding to the temperature change below the thermocline (approximately ~50 m), shown in Figure 7b. Thus, the temperature change in the lower layer could be attributed to the typhoon-induced vertical advection cooling—i.e., upwelling of the cold water. On the other hand, as shown in Figure 7f, the vertical diffusion caused cooling in the mixed layer over the looping area of the typhoon. The results of this diagnostic analysis of the rate of temperature change indicate that the typhoon-induced strong winds caused strong vertical mixing in the mixed layer and intense upwelling below the mixed layer at the center of the typhoon, resulting in a deepening of the mixed layer and mixing between the upwelled cold water and the warm surface water. Through these dynamics, the typhoon presumably upwelled cold, nutrient-rich waters from below the mixed layer up to the mixed layer, which in turn pumped sufficient nutrient fuels for photosynthetic activity via vertical mixing in the euphotic zone, thereby causing a phytoplankton bloom at the sea surface.

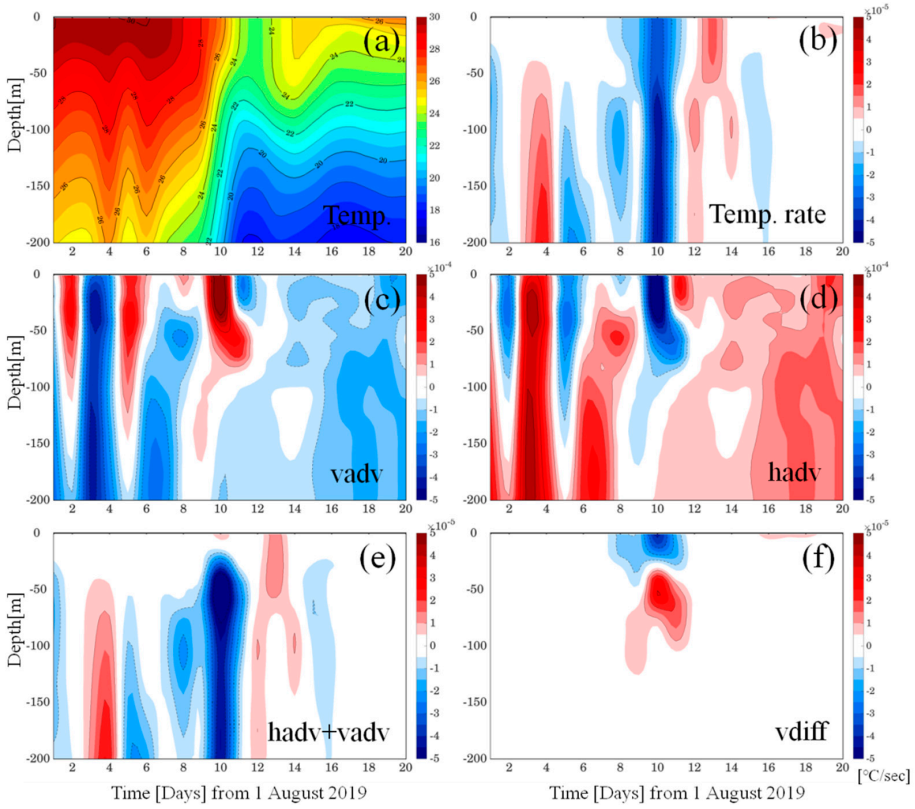

Figure 7. Time–depth diagram of model simulated at the looping area (140.5~141.5E, 22.0~22.5N) of the typhoon (**a**) temperature, (**b**) temperature change rate term, (**c**) vertical advection term, (**d**) horizontal advection term, (**e**) sum of horizontal and vertical advection terms, and (**f**) vertical diffusion term.

5. Conclusions

Remote-sensed SST and Chl-a data reveal the occurrence of a surface phytoplankton bloom with high Chl-a concentrations in a cold eddy in the northwestern Pacific following the passage of Typhoon Krosa in August 2019. In this paper, we discussed the mechanisms producing high surface Chl-a concentrations during typhoon passage and explained the role of physical processes associated with ocean circulation. To investigate the enhancement of Chl-a concentration and the associated upper-ocean conditions before and after typhoon passage, we characterized the surface Chl-a concentration and pre-existing ocean conditions using multiple satellite datasets and Argo measurements and then compared these with the output of a regional ocean circulation model.

Because of the typhoon, the surface Chl-a concentrations in the region increased sharply to more than five times their pre-typhoon values and persisted for approximately two weeks following passage. The elevated post-typhoon concentrations of Chl-a coincided with a pre-existing oceanic cyclone that was detected as an altimetry-based SSHA. The typhoon looped around the oceanic cyclone for one day at speeds of less than 4 m/s, producing an unusual sea surface cooling of up to ~8 °C in the cyclonic eddy region. Our model successfully captured the typhoon-enhanced cold-core cyclonic circulation corresponding to the region of high Chl-a concentration. The model–data comparisons demonstrated that the looping motion of the slow-moving typhoon enhanced a pre-existing cyclonic circulation, resulting in strong vertical mixing and upwelling. A diagnostic analysis of the temperature rate equation confirmed that the typhoon-induced strong winds caused strong vertical mixing in the mixed layer and intense upwelling below the mixed layer at the center of the typhoon, resulting in a deepening of the mixed layer and mixing between the upwelled cold water with the warm surface water. This upwelling of nutrient-rich waters to the mixed layer fueled the photosynthetic activities in the well-mixed euphotic zone and triggered a phytoplankton bloom. The importance of upwelling on the phytoplankton blooms has been well established by several studies, particularly on Karenia brevis, a toxic dinoflagellate that blooms regularly in the Gulf of Mexico [25–28]. Using satellite and ocean observations and/or numerical model results, they showed that the blooms of Karenia brevis along the coasts are closely related with interaction between wind-induced upwelling and concentration of Karenia cells at nearshore frontal boundaries.

These results have significant implications regarding the impact of typhoons on ecosystems in the northwestern Pacific and the importance of typhoons to the carbon fixation process in the oceans [29]. As typhoons increase in strength as a result of global warming, their impacts on the ecosystem and on carbon fixation in the subtropical regions will be increased in the future. Although not a focus of this study, biogeochemical processes can also play an important role in determining the biomass and productivity of the subtropical ocean [13]. Thus, further studies are clearly needed to obtain a better understanding of the physical and biogeochemical processes that potentially influence the oceanic ecosystem on longer time scales.

Author Contributions: Conceptualization, J.-H.M.; Formal analysis, J.-H.L.; Funding acquisition, J.-H.L.; Visualization, J.-H.L.; Writing—original draft, J.-H.L. and J.-H.M.; Writing—review and editing, T.K. All authors have read and agreed to the published version of the manuscript.

Funding: This research was supported by Basic Science Research Program to Research Institute for Basic Science (RIBS) of Jeju National University through the National Research Foundation of Korea (NRF) funded by the Ministry of Education (2019R1A6A1A10072987). J.-H. Moon was supported by a National Research Foundation of Korea (NRF) grant funded by the Korea government (MSIP) (NRF-2019R1A2C1003206).

Acknowledgments: We would like to thank the two anonymous reviewers for their helpful comments on improving the manuscript.

Conflicts of Interest: The authors declare no conflict of interest.

References

1. Yu, Y.; Xing, X.; Liu, H.; Yuan, Y.; Wang, Y.; Chai, F. The variability of chlorophyll-a and its relationship with dynamic factors in the basin of the South China Sea. *J. Mar. Syst.* **2019**, *200*, 103230. [CrossRef]
2. Ryther, J.H.; Yentsch, C.S. The Estimation of Phytoplankton Production in the Ocean from Chlorophyll and Light Data1. *Limnol. Oceanogr.* **1957**, *2*, 281–286. [CrossRef]
3. Falkowski, P.G. The role of phytoplankton photosynthesis in global biogeochemical cycles. *Photosynth. Res.* **1994**, *39*, 235–258. [CrossRef] [PubMed]
4. Watson, R.A.; Zeller, D.; Pauly, D. Primary productivity demands of global fishing fleets. *Fish Fish.* **2013**, *15*, 231–241. [CrossRef]
5. Price, J.F. Upper ocean response to a hurricane. *J. Phys. Oceanogr.* **1981**, *11*, 153–175. [CrossRef]
6. Emanuel, K.A. Thermodynamic control of hurricane intensity. *Nat. Cell Biol.* **1999**, *401*, 665–669. [CrossRef]
7. Son, S.; Platt, T.; Bouman, H.; Lee, N.; Sathyendranath, S. Satellite observation of chlorophyll and nutrients increase induced by Typhoon Megi in the Japan/East Sea. *Geophys. Res. Lett.* **2006**, *33*. [CrossRef]
8. Zhao, H.; Shao, J.; Han, G.; Yang, D.; Lv, J. Influence of Typhoon Matsa on Phytoplankton Chlorophyll-a off East China. *PLoS ONE* **2015**, *10*, e0137863. [CrossRef]
9. Liu, Y.; Tang, D.; Evgeny, M. Chlorophyll Concentration Response to the Typhoon Wind-Pump Induced Upper Ocean Processes Considering Air–Sea Heat Exchange. *Remote Sens.* **2019**, *11*, 1825. [CrossRef]
10. D'Asaro, E.; Black, P.; Centurioni, L.; Harr, P.; Jayne, S.R.; Lin, I.-I.; Lee, C.; Morzel, J.; Mrvaljevic, R.; Niiler, P.; et al. Typhoon-Ocean Interaction in the Western North Pacific: Part 1. *Oceanography* **2011**, *24*, 24–31. [CrossRef]
11. Shibano, R.; Yamanaka, Y.; Okada, N.; Chuda, T.; Suzuki, S.-I.; Niino, H.; Toratani, M. Responses of marine ecosystem to typhoon passages in the western subtropical North Pacific. *Geophys. Res. Lett.* **2011**, *38*, L18608. [CrossRef]
12. Chen, Y.; Tang, D. Eddy-feature phytoplankton bloom induced by a tropical cyclone in the South China Sea. *Int. J. Remote Sens.* **2012**, *33*, 7444–7457. [CrossRef]
13. Yin, X.; Wang, Z.; Liu, Y.; Xu, Y. Ocean response to Typhoon Ketsana traveling over the northwest Pacific and a numerical model approach. *Geophys. Res. Lett.* **2007**, *34*, L21606. [CrossRef]
14. Cheng, L.; Zhu, J.; Sriver, R.L. Global representation of tropical cyclone-induced short-term ocean thermal changes using Argo data. *Ocean Sci.* **2015**, *11*, 719–741. [CrossRef]
15. Lin, S.; Zhang, W.-Z.; Shang, S.; Hong, H.-S. Ocean response to typhoons in the western North Pacific: Composite results from Argo data. *Deep Sea Res. Part I Oceanogr. Res. Pap.* **2017**, *123*, 62–74. [CrossRef]
16. Haidvogel, D.B.; Arango, H.G.; Hedstrom, K.; Beckmann, A.; Malanotte-Rizzoli, P.; Shchepetkin, A.F. Model evaluation experiments in the North Atlantic Basin: Simulations in nonlinear terrain-following coordinates. *Dyn. Atmos. Oceans* **2000**, *32*, 239–281. [CrossRef]
17. Shchepetkin, A.F.; McWilliams, J.C. The regional oceanic modeling system (ROMS): A split-explicit, free-surface, topography-following-coordinate oceanic model. *Ocean Model.* **2005**, *9*, 347–404. [CrossRef]
18. Seo, S.N. Digital 30 sec gridded bathymetric data of Korea marginal seas-KorBathy30s. *J. Korean Soc. Coast. Ocean Eng.* **2008**, *20*, 110–120, (In Korean with English Abstract).
19. Lee, S.-H.; Beardsley, R.C. Influence of stratification on residual tidal currents in the Yellow Sea. *J. Geophys. Res. Space Phys.* **1999**, *104*, 15679–15701. [CrossRef]
20. Fairall, C.W.; Bradley, E.F.; Rogers, D.P.; Edson, J.B.; Young, G.S. Bulk parameterization of air-sea fluxes for Tropical Ocean-Global Atmosphere Coupled-Ocean Atmosphere Response Experiment. *J. Geophys. Res. Space Phys.* **1996**, *101*, 3747–3764. [CrossRef]
21. Warner, J.C.; Sherwood, C.R.; Arango, H.G.; Signell, R.P. Performance of four turbulence closure models implemented using a generic length scale method. *Ocean Model.* **2005**, *8*, 81–113. [CrossRef]
22. Egbert, G.D.; Erofeeva, S.Y. Efficient inverse modeling of barotropic ocean tides. *J. Atmos. Ocean Technol.* **2002**, *19*, 183–204. [CrossRef]
23. Zheng, Z.-W.; Ho, C.-R.; Kuo, N.-J. Importance of pre-existing oceanic conditions to upper ocean response induced by Super Typhoon Hai-Tang. *Geophys. Res. Lett.* **2008**, *35*, 20603. [CrossRef]
24. Sun, L.; Yang, Y.; Fu, Y.-F. Impacts of Typhoons on the Kuroshio Large Meander: Observation Evidences. *Atmos. Ocean. Sci. Lett.* **2009**, *2*, 45–50. [CrossRef]

25. Stumpf, R.P.; Litaker, R.W.; Lanerolle, L.; Tester, P.A. Hydrodynamic accumulation of Karenia off the west coast of Florida. *Cont. Shelf Res.* **2008**, *28*, 189–213. [CrossRef]
26. Soto, I.M.; Muller-Karger, F.E.; Hu, C.; Wolny, J. Characterization of Karenia brevis blooms on the West Florida Shelf using ocean color satellite imagery: Implications for bloom maintenance and evolution. *J. Appl. Remote Sens.* **2016**, *11*, 12002. [CrossRef]
27. Hu, C.; Luerssen, R.; Muller-Karger, F.E.; Carder, K.L.; Heil, C.A. On the remote monitoring of Karenia brevis blooms of the west Florida shelf. *Cont. Shelf Res.* **2008**, *28*, 159–176. [CrossRef]
28. Tomlinson, M.; Stumpf, R.P.; Ransibrahmanakul, V.; Truby, E.W.; Kirkpatrick, G.J.; A Pederson, B.; A Vargo, G.; A Heil, C. Evaluation of the use of SeaWiFS imagery for detecting Karenia brevis harmful algal blooms in the eastern Gulf of Mexico. *Remote Sens. Environ.* **2004**, *91*, 293–303. [CrossRef]
29. Wang, T.; Li, D.; Gao, L.; Zhu, L. Estimation of biophysical properties of areas in the Western North Pacific with a high frequency of tropical cyclones. *Deep Sea Res. Part I Oceanogr. Res. Pap.* **2019**, *147*, 12–21. [CrossRef]